Supporting information

Defective polymer carbon nitride with expanding π-electron domains for efficient photocatalytic H_2 evolution

Yujie Liang[a], Lina Wu[b,*], Lei Zeng[c,*], Yabin Jiang[a,*]

[a] Precision Medicine Laboratory for Chronic Non-communicable Diseases of Shandong Province, Institute of Precision Medicine, Jining Medical University, Jining, 272067, P. R. China

[b] Jilin Provincial Key Laboratory of Western Jilin's Clean Energy, Baicheng Normal University, Baicheng 137000, P. R. China.

[c] School of Chemical Engineering and Pharmacy, Hubei Key Lab of Novel Reactor & Green Chemical Technology, Key Laboratory of Green Chemical Engineering Process of Ministry of Education, Wuhan Institute of Technology, No.206 Guanggu Road, East Lake New Technology Development Zone, Wuhan, 430072, P. R. China.

Corresponding Author
*E-mail: wuln@bcnu.edu.cn; zl0613341@sina.com; jiang01357@163.com

1.1 Experimental Section

The CNBD was synthesized via a two-step procedure. Initially, 1 g of dicyandiamide was mixed with 30 mg of 1,2-dicyanobenzene, ground, and heated at 550°C for 2 hours with a heating rate of 5°C/min in a covered crucible. After cooling to room temperature, the sample was further ground. Subsequently, a second annealing process was conducted at 550°C for 2 hours in a hydrogen atmosphere (5% H_2/95% Ar) with a heating rate of 5°C/min. The resulting solid was ground in an agate mortar and labeled as CNBD. CND was obtained using the same procedure but without the addition of 1,2-dicyanobenzene. CNB was only prepared by calcining dicyandiamide and 1,2-dicyanobenzene at 550 °C for 2 hours in a muffle furnace with a heating rate of 5°C/min. For comparison, pristine PCN powder (CN) was synthesized under the same conditions as CNB but without the addition of 1,2-dicyanobenzene.

1.2 Characterization

Scanning electron microscopy (SEM) images were acquired using a Hitachi S4800 field emission scanning electron microscope. Transmission electron microscope (TEM) images for analyzing sample morphology and elements were obtained with a Talos F200X from FEI. Powder X-ray diffraction (XRD) patterns were recorded on a Bruker diffractometer using Cu Kα (λ = 0.15406 nm) radiation. Fourier transform infrared spectroscopy (FTIR) spectra were collected with a Thermo Scientific Nicolet iS10 spectrometer. UV-visible (UV-Vis) diffuse reflectance spectra (DRS) were measured using a Shimadzu UV-2450 spectrophotometer equipped with an integrating sphere, and subsequently converted to absorption spectra using Kubelka-Munk transformation. Brunauer-Emmett-Teller (BET) surface areas and pore size distributions were determined using a JW-BK100B instrument. X-ray photoelectron spectroscopy (XPS) spectra were acquired on a Thermo ESCALAB 250Xi spectrometer. X-ray absorption near-edge structure (XANES) spectroscopy measurements at C and N K-edges were conducted at BL11U in the National Synchrotron Radiation Laboratory, Anhui, China. Elemental analysis (EA) of carbon, nitrogen, and hydrogen content was performed using an elemental analyzer (Elementar, VARIO EL III). Electron paramagnetic

resonance (EPR) tests were conducted on a Bruker A300 ESR spectrometer. Photoluminescence (PL) spectra were measured with an Edinburgh instrument (FLSP 920, λ_{Ex}=325 nm), and time-resolved PL spectra were obtained using an FLS 1000. Photocurrent measurements, electrochemical impedance spectroscopy (EIS), and Mott-Schottky plots were carried out using an electrochemical analyzer (Shanghai, Chen Hua, CHI660E).

1.3 Photocatalytic H_2 Production

The photocatalytic hydrogen evolution reactions were conducted using a PerfectLight reaction system connected to a closed gas circulation and evacuation setup, illuminated by a 300 W Xe lamp with a cut-off filter ($\lambda > 420$ nm). 0.1 g of photocatalyst was dispersed in a 100 mL aqueous solution containing 20 vol. % triethanolamine (TEOA) as a sacrificial agent, achieved through sonication. Prior to irradiation, the reactor was thoroughly evacuated using a vacuum pump to remove dissolved air from the water. The amount of evolved H_2 was analyzed using online gas chromatography with a TCD detector (Shimadzu Corp., Japan, GC-8A, argon as the carrier gas). Pt co-catalyst (3 wt%) for enhancing hydrogen evolution was in situ photo-deposited on the photocatalyst using $H_2PtCl_6 \cdot 6H_2O$ (3 ml, 1 mg ml^{-1} of Pt) as a precursor. The temperature during all photocatalytic reactions was maintained at 25 °C ± 5 °C.

1.4 Calculation methods

All first - principles calculations were performed using the Vienna ab initio simulation package (VASP). The projected augmented wave (PAW) method was employed to characterize the electron - ion interactions, and the generalized gradient approximation (GGA) of the Perdew - Burke - Ernzerhof (PBE) functional was utilized for the exchange - correlation interactions. Additionally, Grimme's DFT - D3 correction method was adopted to account for van der Waals (vdW) interactions. For all models, a 2×3×1 Monkhorst - Pack k - point grid was used to sample the Brillouin Zone in all calculations, with the plane - wave energy cutoff set at 400 eV. The energy convergence

criterion for lattice vectors was 10^{-5} eV, and the force convergence criterion for atomic positions was 0.02 eV·Å^{-1}. The Gibbs free energy changes (ΔG) during the hydrogen evolution reaction (HER) of the materials were calculated using the concept of the computational materials proposed by Nørskov et al.

The photocatalytic water splitting reaction of the materials was modeled following the approach reported by Nørskov et al. [1]. In an aqueous environment, the HER mechanism involves two sequential one-electron transfer steps, with each step consuming one proton and one electron:

Step 1: $* + H^+ + e^- = H*$

Step 2: $H* + H^+ + e^- = * + H_2$

The Gibbs free energy was computed using the equation G(T)=E+H(T)−TS(T), where Erepresents the self-consistent field energy of the species, incorporating all temperature-dependent contributions to the enthalpy H(T) and entropy S(T). Specifically, for gas-phase species, vibrational, rotational, and translational degrees of freedom were included, whereas for adsorbed species, only vibrational contributions were considered due to the restricted rotational and translational motions [2]. Consequently, the Gibbs free energy change ΔG under an external potential U for the aforementioned steps can be derived using the subsequent equation:

$\Delta G1 = G(H*) - G(*) - 1/2G(H_2) - eU_e$

$\Delta G2 = G(*) + 1/2G(H_2) - G(H*) - eU_e$

For photocatalytic reactions, the U_e are the HER potentials. Where U_e are the energy difference between CBM relative to the hydrogen reduction potential (H^+/H_2).

Reference:

[1] Skúlason E, Karlberg G S, Rossmeisl J, et al. Density functional theory calculations for the hydrogen evolution reaction in an electrochemical double layer on the Pt (111) electrode [J]. *Physical Chemistry Chemical Physics*, 2007, 9(25): 3241-3250.

[2] Nørskov J K, Rossmeisl J, Logadottir A, et al. Origin of the overpotential for oxygen reduction at a fuel-cell cathode [J]. *The Journal of Physical Chemistry B*, 2004, 108(46): 17886-17892.

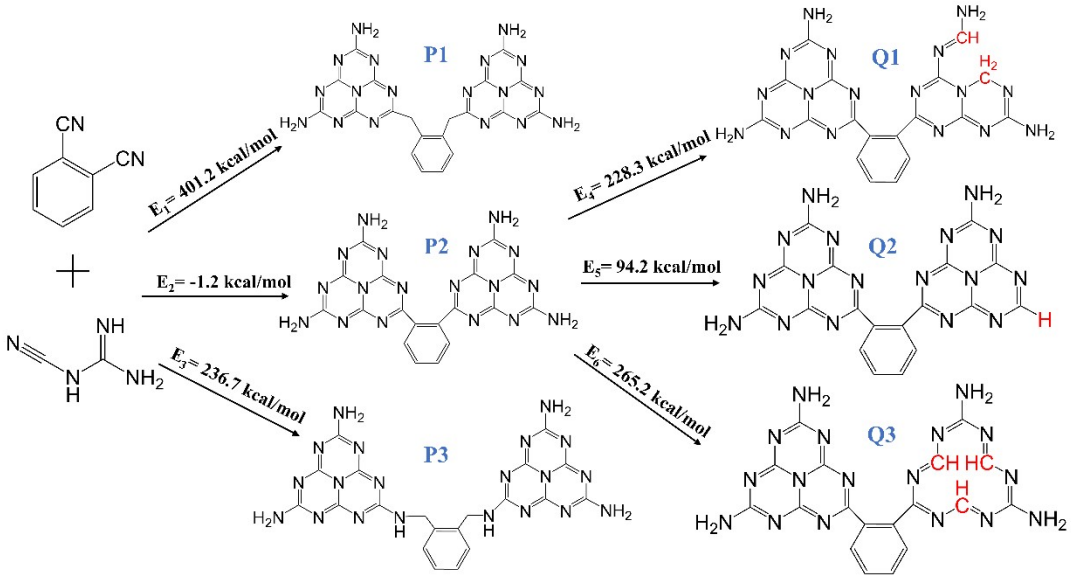

Fig. S1. The calculated gibbs free energy (ΔG) of dicyandiamide and 1,2-dicyanobenzene.

The DFT simulation calculated the binding reaction of dicyandiamide and 1,2-dicyanobenzene. Dicyandiamide was transformed to melamine via thermal condensation. The carbon atom near the cyano groups of 1,2-dicyanobenzene is high of electrophilicity and prone to react with amino groups in the melamine molecule. As shown in Fig. S1, in the first step of thermal polymerization reaction, the Gibbs Free Energy (ΔG) of P2 is the lowest. After the second step of hydrogen treatment, Q2 also had the lowest ΔG, so we also determined the molecular structure of CNBD.

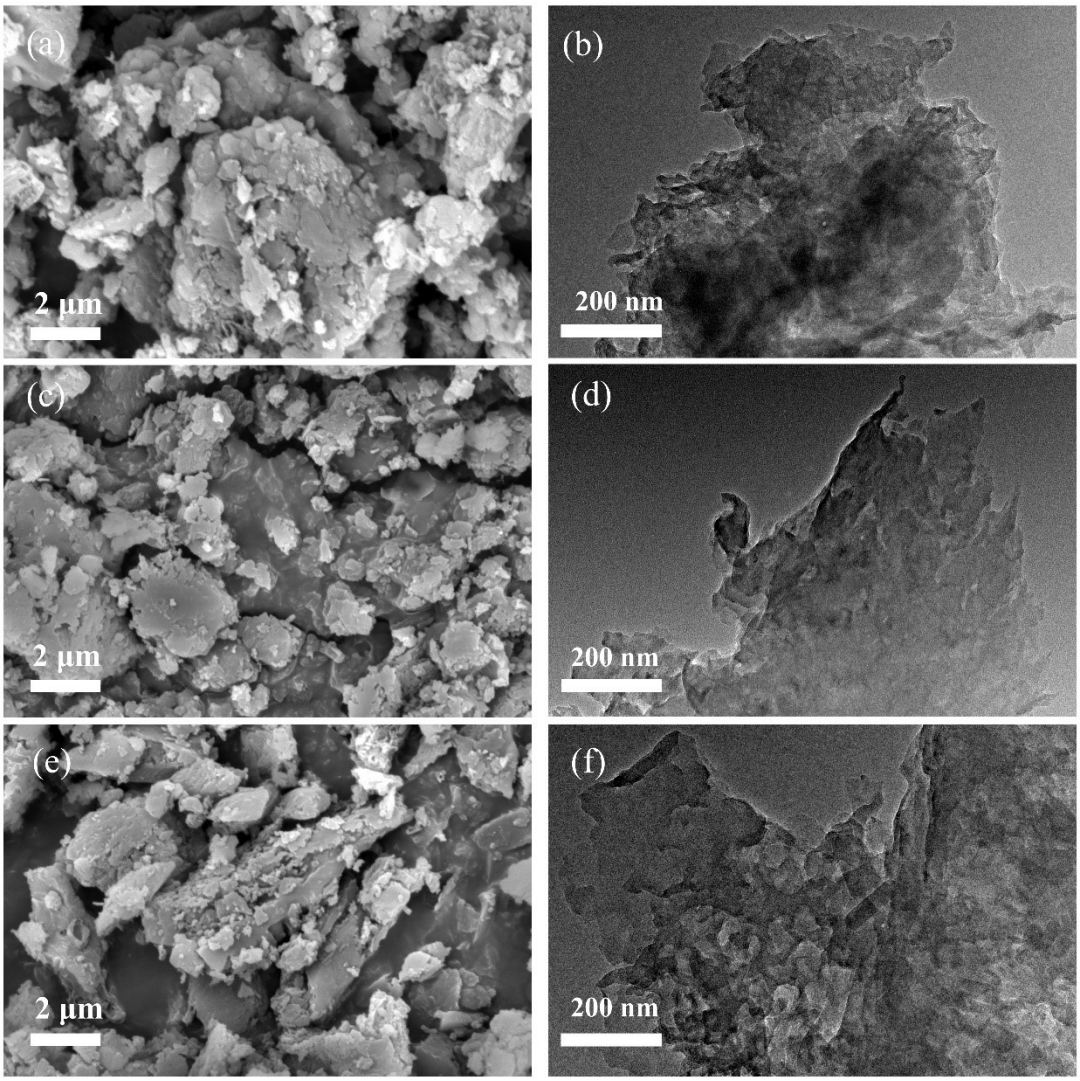

Fig. S2. SEM images of CN (a), CNB (c), CND (e) and TEM images of CN (b), CNB (d), CND (f).

The morphology of CNB and CND was analyzed by SEM and TEM. In comparison with CN, CNB exhibits lamellar stacked nanostructures, whereas CND shows the presence of porous features. TEM images clearly visualize the sheet-like nanostructures in both CNB and CND; moreover, CND presents a relatively looser architecture compared to CNB.

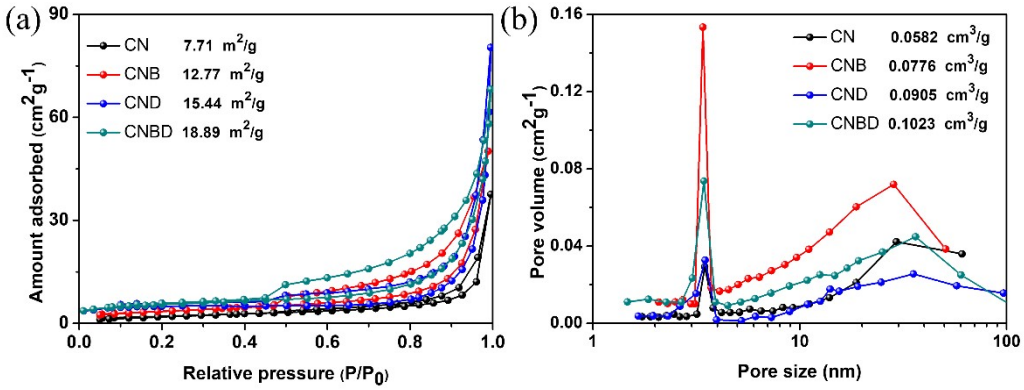

Fig. S3. (a) N_2 adsorb/desorption isotherms and (b) the pore size distribution of CN, CNB, CND and CNBD.

As illustrated in Fig. S3, all tested samples display type IV isotherms with H3-type hysteresis loops, revealing their mesoporous characteristics with unevenly distributed pores. The BET surface areas of CNB and CND are approximately 12.77 and 15.44 m^2/g, respectively. Compared to CN, CNB and CND exhibit higher BET surface areas, indicating that both the addition of 1,2-dicyanobenzene and hydrogen thermal treatment can enhance the surface area of polymeric carbon nitride—an attribute beneficial for photocatalytic H_2 evolution. The pore volumes of CNB and CND are 0.0776 and 0.0905 cm^3/g, respectively. The increased surface area facilitates mass transfer, thereby promoting the improvement of photocatalytic activity.

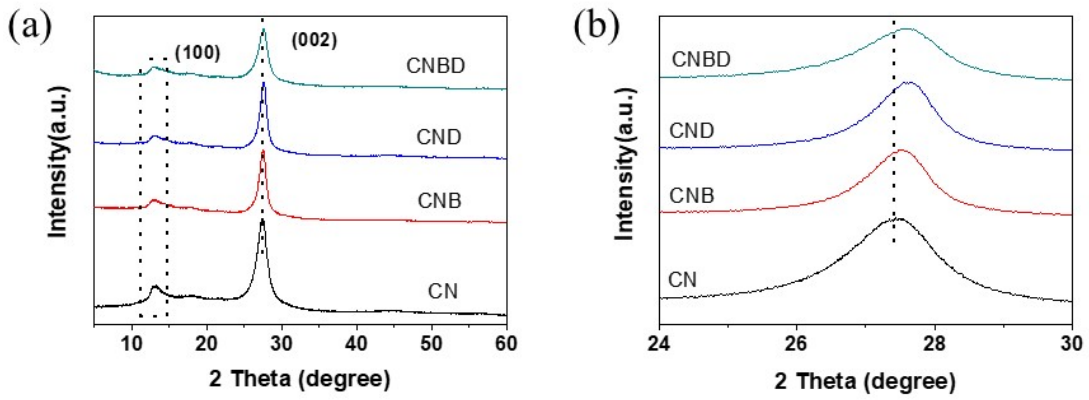

Fig. S4. (a) XRD patterns and (b) locally amplified XRD patterns of CN, CNB, CND and CNBD.

According to the XRD patterns in Fig. S4, all synthesized samples displayed two characteristic diffraction peaks corresponding to the (100) and (002) crystal planes, suggesting that the fundamental crystalline framework of polymeric carbon nitride was predominantly preserved after modification. In comparison with the pristine CN, the diffraction peaks of CNB exhibited reduced intensity and broadening, indicating that the incorporation of benzene rings disrupted the long-range ordered structure of the CN lattice. Notably, samples CND and CNBD, which were subjected to thermal treatment under a hydrogen atmosphere, showed significantly decreased peak intensities, a phenomenon attributed to the elimination of nitrogen-containing moieties from the CN skeleton. This structural modification likely reduced interlayer repulsive forces and enhanced interlayer stacking density, as evidenced by the altered diffraction characteristics.

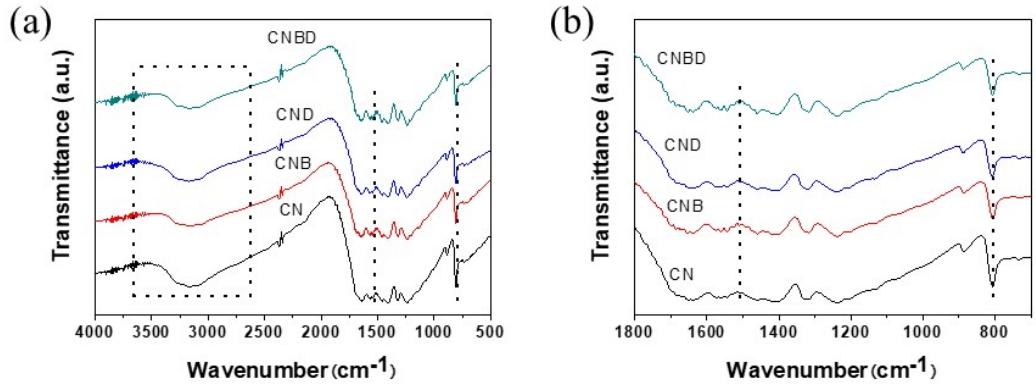

Fig. S5. (a) FT-IR spectra and (b) locally amplified FT-IR patterns of CN, CNB, CND and CNBD.

As illustrated in Fig. S5, the FT-IR spectra of CN, CNB, CND, and CNBD all exhibit characteristic absorption bands typical of polymeric carbon nitride. Specifically, a broad absorption band in the range of 2900–3500 cm^{-1} is attributed to the stretching vibrations of -NH_2 groups or adsorbed water molecules. A series of intense peaks in the 1200–1600 cm^{-1} region is assigned to the skeletal vibrations of C–N heterocycles, while a prominent absorption at 810 cm^{-1} corresponds to the in-plane bending vibrations of triazine units. Notably, compared with CN and CND, the spectra of CNB and CNBD display a subtle additional absorption band at approximately 1538 cm^{-1}, which can be attributed to the in-plane stretching vibration of aromatic rings. For the hydrogen-treated samples (CND and CNBD), the vibrational absorptions associated with NH_2 groups in the 2900–3500 cm^{-1} region were attenuated, suggesting the presence of nitrogen vacancies in the polymeric carbon nitride framework. This spectral feature indicates that thermal treatment under hydrogen atmosphere induced the elimination of amino moieties, leading to structural modifications in the carbon nitride lattice.

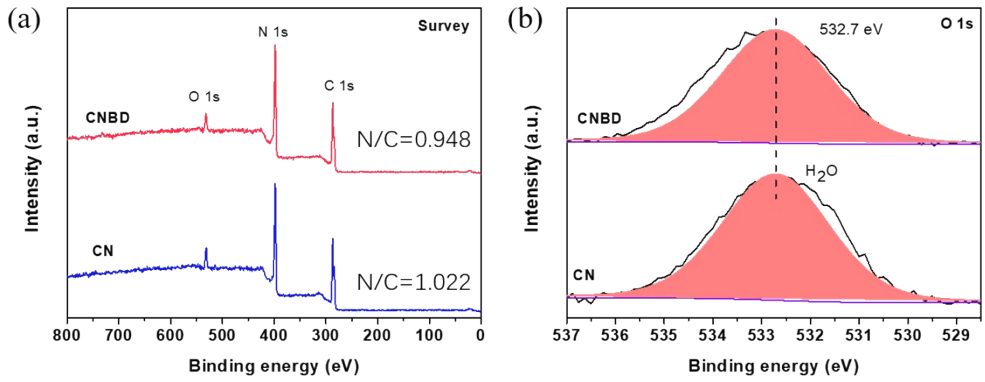

Fig. S6. (a) total XPS survey spectra and (b) O1s of CN and CNBD.

XPS-derived N/C ratios atomic ratios of 1.022 for CN and 0.948 for CNBD (Fig. S6a), consistent with the incorporation of benzene rings and nitrogen vacancies into the polymer carbon nitride framework. This trend was corroborated by elemental analysis (EA) yielded N/C, which exhibited an analogous decrease in CNBD relative to CN (Table S1). Fig. S6b presents the fitted O1s XPS spectra of CN and CNBD. Both CN and CNBD samples exhibit one peak at 523.7 eV, which is associated with the surface adsorbed adventitious oxygen-containing species, for example, CO_2 and H_2O.

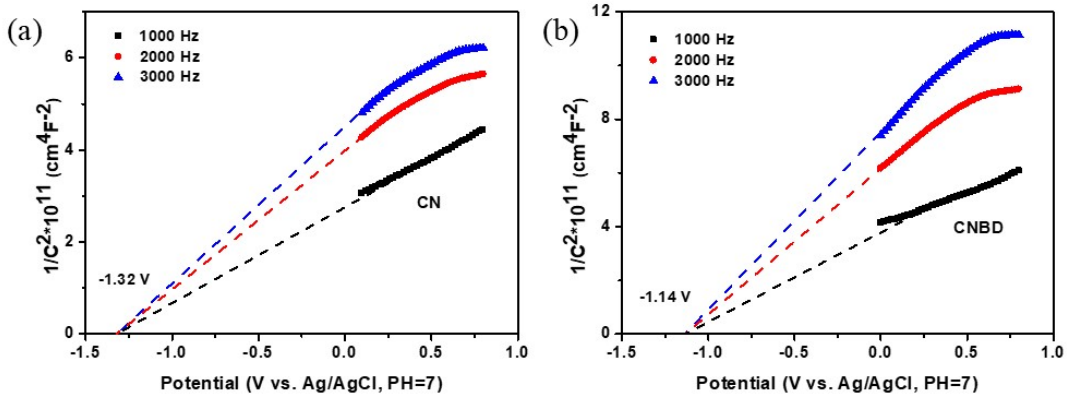

Fig. S7. Mott-Schottky plots of (a) CN and (b) CNBD.

The flat-band potentials of CN and CNBD are calculated to be ca. -1.32 V and ca. -1.14 V vs. Ag/AgCl at pH = 7.0, which correspond to ca. -0.71 V and ca. -0.53 V vs. Normal hydrogen electrode (NHE) at pH = 7.0, respectively

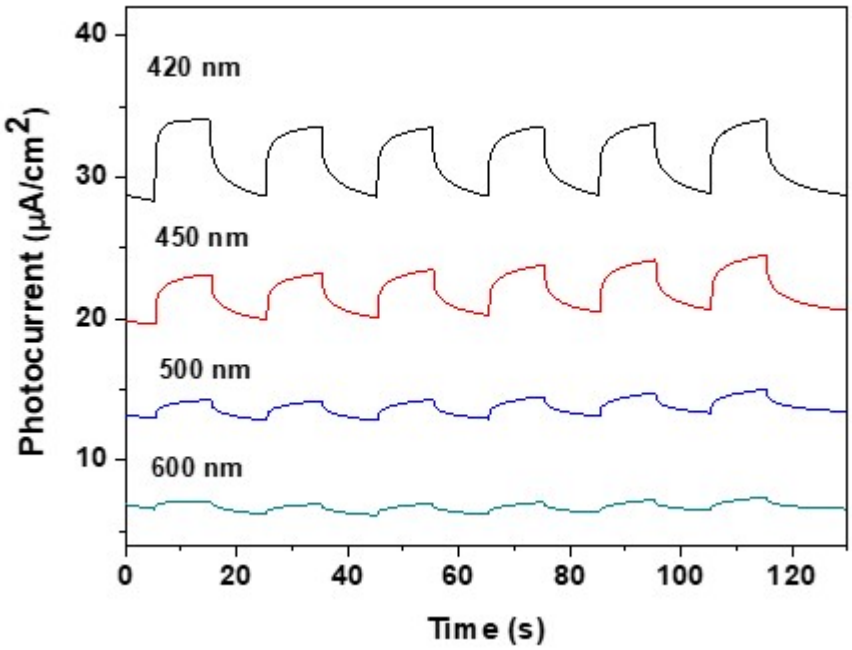

Fig. S8. Photocurrent response curves of CNBD under different fixed wavelength lights.

The CNBD electrode generates measurable photocurrent responses across a broad spectral range (420-600 nm; Fig. S8), with photocurrent density diminishing as wavelength increases. Significant photocurrent generation persists even at 600 nm, highlighting the extended visible-light harvesting capacity of CNBD. The enhanced photocurrent density and widened spectral response collectively demonstrate that the synergistic presence of benzene rings and nitrogen vacancies within the PCN matrix promotes interfacial charge transfer and separation. This enhancement facilitates improved utilization of incident light energy, thereby elevating photocatalytic hydrogen evolution performance.

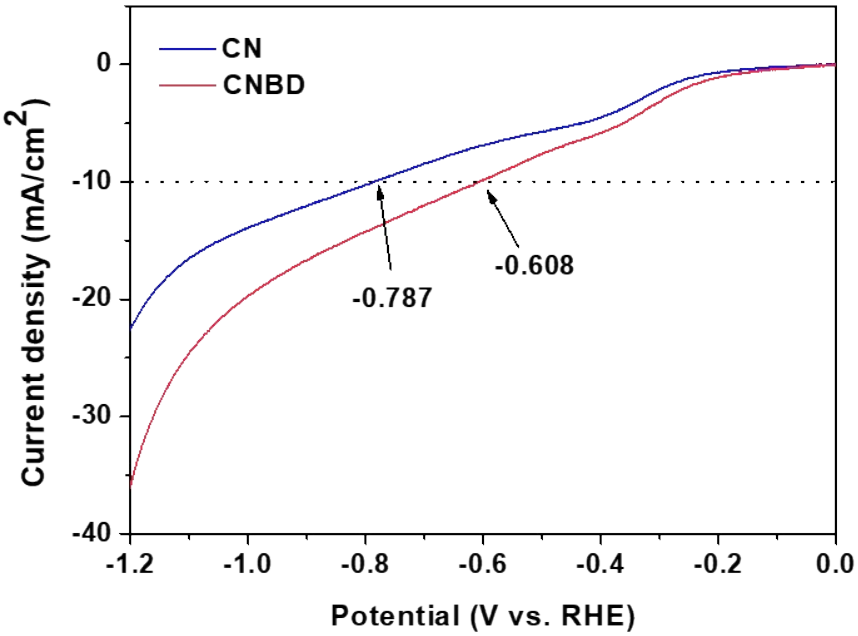

Fig. S9. Polarization curves of CN and CNBD.

Complementary linear sweep voltammetry (LSV) polarization curves (Fig. S9) indicate that CNBD achieves a current density of 10 mA cm^{-2} at a substantially lower overpotential (-0.608 V) than pure CN (-0.787 V). This substantial difference in overpotential implies enhanced electrocatalytic suitability of CNBD for the hydrogen evolution reaction (HER).

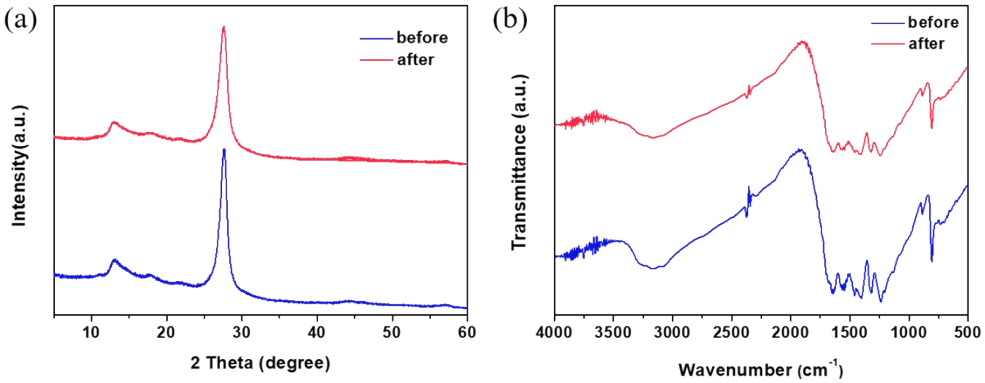

Fig. S10. (a) XRD patterns and (b) FT-IR spectra before and after cycles of CNBD.

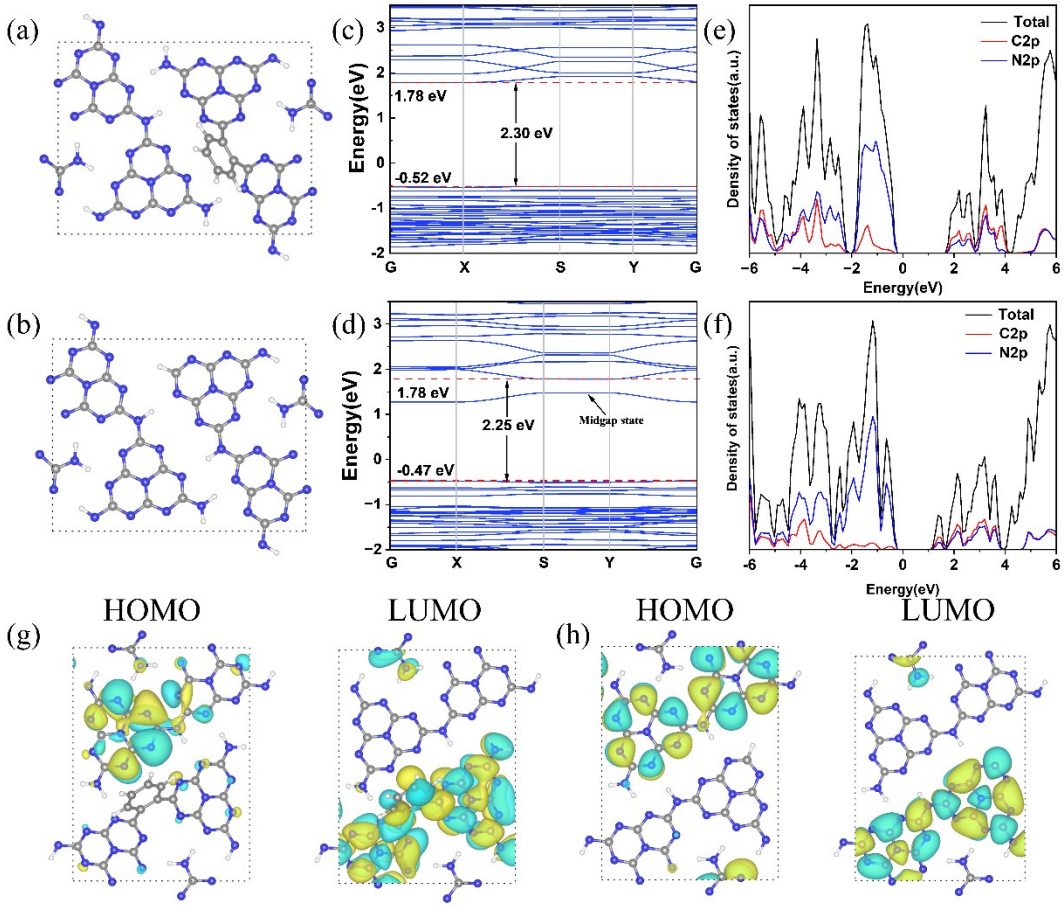

Fig. S11. Structure models of (a) CNB and (b) CND. Calculated band structures and corresponding DOS of (c, e) CNB and (d, f) CND. HOMO and LUMO energy levels of (g) CNB and (h) CND.

The specific contributions of benzene ring doping and nitrogen vacancy can be analyzed via the corresponding orbital-resolved DOS (Fig. S11). Upon doping of benzene rings into the PCN framework, the contribution of C 2p orbitals to the CB composition increases, indicating an improvement in electronic conjugation due to the incorporation of benzene rings, which leads to a downward shift of the CB position. DOS analysis further reveals that nitrogen vacancy defects introduce the midgap state within the bandgap between the VB and CB. Beyond modulating the band structure, the incorporation of benzene ring dopants and nitrogen vacancy defects also exerts a significant influence on the separation efficiency of photoexcited charge carriers.

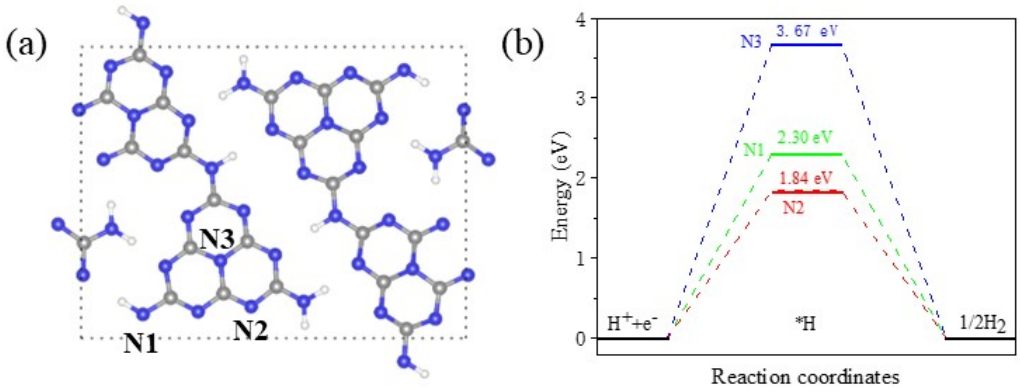

Fig. S12. (a) The H*optimal adsorption on the three N active sites of CN, (b) Free energy diagram of HER on CN.

Initially, density functional theory (DFT) calculations were employed to simulate the optimized atomic configurations of CN, as depicted in Fig. S12. The intrinsic hydrogen evolution reaction (HER) catalytic activities were evaluated by calculating the ΔG_{H^*} values of CN. The adsorption of H* active intermediates on three distinct N active sites of CN was meticulously optimized. Calculation results indicated that the ΔG_{H^*} values of CN at the three N active sites were determined to be 2.30 eV (N1), 1.84 eV (N2), and 2.67 eV (N3), respectively. Notably, the ΔG_{H^*} value of CNBD at the N vacancy site was calculated to be 0.37 eV, which is remarkably close to the ideal zero value, in stark contrast to the ΔG_{H^*} value of CN at the N2 site. These DFT findings unambiguously confirm that the introduction of N vacancies into polymer carbon nitride plays a pivotal role in enhancing the HER catalytic performance.

Table S1. EA of CN, CNB, CND and CNBD.

Samples	N wt.%	C wt.%	H wt.%	N/C	H/C
CN	65.52	34.87	1.955	1.879	0.056
CNB	62.93	35.04	1.857	1.796	0.053
CND	61.6	34.27	1.901	1.797	0.055
CNBD	62.99	35.25	1.761	1.787	0.050

As presented in Table S1, the mass ratio of nitrogen to carbon (N/C) in CNB is lower than that in CN; correspondingly, the mass ratio of hydrogen to carbon (H/C) in CNB also exhibits a lower value compared with CN. These findings demonstrate that a polycondensation reaction takes place between the cyano groups of 1,2-dicyanobenzene and dicyandiamide. Within the CNB framework, the benzene ring establishes a connection with nitrogen (N) atoms through the elimination of NHx groups. Elemental analysis (EA) was employed to characterize the defect types in CND. The results reveal that the N/C mass ratio of CND is lower than that of CN, which directly provides evidence for the existence of nitrogen vacancy defects in the CND framework. Furthermore, a comparison of the H/C mass ratios between CND and CN offers additional support for the conclusion that nitrogen defects in CND primarily originate from the deficiency of NH_x species, a phenomenon induced by hydrogen treatment. On this basis, CNBD was synthesized via a two-step process: first, the thermal condensation of 1,2-dicyanobenzene and dicyandiamide under an air atmosphere; subsequently, a treatment of the resulting product in a hydrogen (H_2) atmosphere under the same temperature and duration conditions. As shown in Table S1, both the N/C and H/C mass ratios of CNBD are lower than those of CN. This observation implies two key structural features of CNBD: (1) the amino groups within the material act as linkers to connect heptazine oligomers through benzene rings; (2) the nitrogen vacancy defects in CNBD are mainly derived from the deficiency of NHx groups. Importantly, these results are consistent with the findings obtained from X-ray

photoelectron spectroscopy (XPS) analysis, further validating the structural characteristics of CNBD proposed herein.

Table S2. Relative ratios of C=C, N-C=N and C-NH_X determined by C1s spectra.

Samples	C=C %	N-C=N %	C-NH_X %
CN	28.62	62.79	8.59
CNBD	32.49	59.64	7.87

Table S3. Relative ratios of C-N=C, N-$(C)_3$ and C-NH_X determined by N1s spectra.

Samples	C-NH_X %	N-$(C)_3$ %	C-N=C %
CN	10.43	25.96	63.61
CNBD	9.31	28.17	62.52

Table S4. The fitted fluorescence components of CN and CNBD, respectively.

Materials	Decay time/ns		Relative amplitude/%		Average
	τ1	τ2	A1	A2	lifetime/ns
CN	1.46	6.16	1258.76	1067.08	5.13
CNBD	0.93	4.38	1677.98	820.34	3.33